

Adaptive target detection with application to¹ Through-the-Wall Radar Imaging

Christian Debes[†], Jesper Riedler[†], Abdelhak M. Zoubir[†] and Moeness G.
Amin[‡]

[†] Signal Processing Group, Institute of
Telecommunications
Technische Universität Darmstadt
Merckstr. 25
64283 Darmstadt, Germany
E-mail: {cdebes, jriedler, zoubir}@spg.tu-darmstadt.de

[‡] Radar Imaging Lab, Center for Advanced
Communications
Villanova University
800 Lancaster Ave.
Villanova PA 19085, USA
E-mail: moeness.amin@villanova.edu

Abstract

An adaptive detection scheme is proposed for radar imaging. The proposed detector is a post-processing scheme derived for one-, two- and three dimensional data, and applied to Through-the-Wall imaging using synthetic aperture radar. The target image statistics depend on the target three-dimensional orientation and position. The statistics can also vary with the standoff distance of the imaging system because of the change in the corresponding scene image resolution. We propose an iterative target detection scheme for the cases in which no or partial a priori knowledge of the target image statistics is available. Properties of the proposed scheme, such as conditions of convergence and optimal configurations are introduced. The detector performance is examined under synthetic and real data. The latter is obtained using a synthetic aperture Through-the-Wall radar indoor imaging scanner implementing wideband delay and sum beamforming.

Keywords: Detection theory, Through-the-wall, radar imaging,

I. INTRODUCTION

In synthetic and physical aperture radar imaging applications [1], [2], there is a need for robust target detection schemes. In many applications, such as Through-the-Wall Radar Imaging (TWRI) [3], [4], [5], [6], [7], [8], there is generally a large number of possible indoor targets which might assume different sizes and shapes. Additionally, limited signal bandwidth due to wall attenuation issues [9] does not permit fine target resolution, rendering target recognition and detection difficult to achieve. When examining and analyzing images, it is found that the image statistics, even for the same target and background scene, may

significantly vary depending on the target range and cross-range values [10]. A practical² detector, applied in the image domain, must then perform satisfactorily under changing and unknown target statistics. The changes in target statistics from presumed or reference values might be attributed to a change in either the imaging system or/and in the imaged target. The former stems from a change in the receiver noise level and could be also a result of a modification in the system standoff distance [11], which induces different image fidelity and resolution. The latter, on the other hand, could be a consequence of unknown target orientation. These variations induce ambiguities in target image intensity and distribution, rendering prior knowledge of a reference probability density function (pdf) of the target insufficient for its detection.

One way to address this problem is the use of constant false-alarm rate (CFAR) detectors [12], [13] which aim at providing a constant false-alarm rate while the statistics may be space- and/or time-varying. The drawback of these approaches is that important parameter such as cell size and guard cell size in cell-averaging CFAR [14] or the percentile in order-statistics CFAR [12], [15] has to be chosen beforehand, which have a strong impact on the detection result. In [10], we presented a target detection approach that iteratively adapts to varying statistics which has been successfully applied in detection of targets behind walls. At the core of the detector in [10], an image processing step is used which aims at separating target and noise data. Improved detection was achieved by replacing the static two-dimensional filtering in [10] by morphological operations [16]. However, these filtering operations are not self-learning and require fixed pre-set values, which may not be the most suitable for the underlying image. A procedure of how to choose the optimal filtering step, given the image data, is, therefore, required for a full automation of the detection process.

The contribution of this paper is to derive properties of the iterative detection approach [10], [16], such as bias and conditions of convergence. Based on this, an optimization approach is presented to allow for optimal configuration of the iterative detector. We consider detection of stationary targets as opposed to the detection of moving targets [17], [18], [19] where Doppler shifts can be considered.

The paper is organized as follows. In Section II, a simple iterative detection approach is presented. It is motivated and derived for one-dimensional signals. We show that the

simple iterative detection approach generally provides biased parameter estimates and, thus,³ does not achieve the required false-alarm rate. In Section III, morphological filtering is presented as an extension to the simple iterative detection approach. The optimal choice of the morphological filter is discussed in details. An optimization algorithm to find the optimal filtering operation is presented in Section IV. In order to assess the performance of the presented approaches, simulation results using one dimensional signals are shown in Section V. Further, to demonstrate its usability in practice, the iterative detection approach is applied to TWRI images in Section VI. Here, the concepts of the proposed detector are extended to two- and three dimensional signals and can thus be applied to TWRI radar B-Scans or complete three dimensional TWRI images. Finally, Section VII provides conclusions.

II. AN ITERATIVE DETECTION APPROACH

Assume a one-dimensional signal $x(n)$, $n = 0, \dots, N-1$, which consists of target and noise samples. The aim is to obtain a binary signal $b(n)$, $n = 0, \dots, N-1$, which describes the presence and absence of targets, i.e.

$$b(n) = \begin{cases} 1, & \text{target is present at time } n \\ 0, & \text{target is absent at time } n \end{cases} \quad (1)$$

The data $x(n)$ could represent one line or column in a radar image, and, as such, consists of different, spatially isolated regions or groups. Target detection in the image domain, e.g., based on the Neyman-Pearson test [20] can proceed by assuming each of the data groups (in the simple case: target and noise) to be i.i.d. (independent and identically distributed), and by assigning corresponding conditional distribution functions under the null and the alternative hypothesis $p(x|H_0)$ and $p(x|H_1)$, respectively. Hereby, the likelihood ratio (LR) $\frac{p(x|H_1)}{p(x|H_0)}$ is compared to a threshold γ to decide for one of the hypotheses as,

$$\text{LR}(x) = \frac{p(x|H_1)}{p(x|H_0)} \underset{H_0}{\overset{H_1}{\gtrless}} \gamma \quad (2)$$

where γ can be obtained by setting a false-alarm rate α and solving for

$$\alpha = \int_{\gamma}^{\infty} f_L(l|H_0) dl \quad (3)$$

with $f_L(l|H_0)$ being the likelihood ratio distribution under the null hypothesis.

The problem of using a detector, which is based on $p(x|H_0)$ and $p(x|H_1)$, is the need for⁴ having accurate estimates of the density functions under both hypotheses. A possible solution to this problem, applied in the area of TWRI, is considered in [10], [16], where the detector still performs under unknown or varying statistics. A block diagram of a simplified version of the iterative detection approach, presented in [10], [16], is shown in Figure 1. In this approach, the conditional distribution functions $p(x|H_0)$ and $p(x|H_1)$, are characterized by the parameter vectors $\underline{\theta}_0$ and $\underline{\theta}_1$, respectively. Given a nominal false-alarm rate α and initial estimates $\hat{\underline{\theta}}_{0,0}$ and $\hat{\underline{\theta}}_{1,0}$, which can be obtained by using the generalized likelihood ratio test (GLRT) [20], target detection using the Neyman-Pearson test, as described in Equation (2), can be performed. The result of this detection operation is a binary signal $b_0^D(n)$, $n = 0, \dots, N - 1$, where the superscript D stands for 'Detection'. The binary signal can be viewed as a first indication of target and noise samples. That is, it can be used as a mask on the original data $x(n)$, $n = 0, \dots, N - 1$, to sort the data into disjoint target and noise sets. A parameter estimation scheme is then applied on the obtained target and noise sets to provide updated parameter estimates $\hat{\underline{\theta}}_{0,1}$ and $\hat{\underline{\theta}}_{1,1}$. Such schemes can be based on maximum likelihood estimation [21]. The updates are finally forwarded to the detector in order to obtain an improved binary signal $b_1^D(n)$, $n = 0, \dots, N - 1$. The iteration stops when a vanishing difference between subsequent parameter estimates, e.g. $\|\hat{\underline{\theta}}_{0,j} - \hat{\underline{\theta}}_{0,j-1}\|$ and $\|\hat{\underline{\theta}}_{1,j} - \hat{\underline{\theta}}_{1,j-1}\|$ or a vanishing difference between the binary signals, e.g. $\sum_{n=0}^{N-1} |b_j^D(n) - b_{j-1}^D(n)|$ is observed.

The different steps of the above iterative detection approach are detailed below, using two arbitrary conditional distribution functions $p(x|H_0)$ and $p(x|H_1)$. It is noted that, given initial estimates $\hat{\underline{\theta}}_{0,0}$ and $\hat{\underline{\theta}}_{1,0}$ and a pre-set false-alarm rate α , an initial threshold γ_0 can be obtained by evaluating Equation (3).

We assume that the likelihood ratio threshold γ_0 corresponds to a single sample threshold β_0 , i.e., the test can also be applied in the sample domain via $x \underset{H_0}{\overset{H_1}{\gtrless}} \beta$. This assumption is true for e.g. two Gaussian density functions with the same variance. This restriction is not necessary, but simplifies the iterative scheme mathematical descriptions. The target and noise sets in the initial iteration step $j = 0$, \mathcal{T}_0 and \mathcal{N}_0 , are disjoint sets of samples, satisfying,

$$\mathcal{T}_0 = \{x(n)|x(n) > \beta_0\}; \quad \mathcal{N}_0 = \{x(n)|x(n) < \beta_0\} \quad (4)$$

The distributions of the so obtained noise and target data are expressed as,

$$f_{0,0}(x) = A_{0,0} \cdot [(1 - \epsilon)p(x|H_0) + \epsilon p(x|H_1)]; \quad x < \beta_0 \quad (5)$$

$$f_{1,0}(x) = A_{1,0} \cdot [(1 - \epsilon)p(x|H_0) + \epsilon p(x|H_1)]; \quad x > \beta_0 \quad (6)$$

where ϵ denotes the probability of target occurrence and $A_{0,0}$ and $A_{1,0}$ are scaling factors fulfilling,

$$\int_{-\infty}^{\infty} f_{0,0}(x) dx = \int_{-\infty}^{\beta_0} f_{0,0}(x) dx = 1 \quad (7)$$

$$\int_{-\infty}^{\infty} f_{1,0}(x) dx = \int_{\beta_0}^{\infty} f_{1,0}(x) dx = 1 \quad (8)$$

In the following, the parts of the pdfs resulting from false-alarms and missed detection are defined as,

$$p_0^{FA}(x) = p(x|H_0); \quad x > \beta_0 \quad (9)$$

$$p_0^{MD}(x) = p(x|H_1); \quad x < \beta_0 \quad (10)$$

Consequently, the true noise and target distributions $p(x|H_0)$ and $p(x|H_1)$ can be written as,

$$p(x|H_0) = \frac{1}{1 - \epsilon} \left[\frac{f_{0,0}(x)}{A_{0,0}} - \epsilon p_0^{MD}(x) \right] + p_0^{FA}(x) \quad (11)$$

$$p(x|H_1) = \frac{1}{\epsilon} \left[\frac{f_{1,0}(x)}{A_{1,0}} - (1 - \epsilon) p_0^{FA}(x) \right] + p_0^{MD}(x) \quad (12)$$

Within the j -th iteration of the proposed iterative detection algorithm, updated estimates $\hat{\underline{\theta}}_{0,j}$ and $\hat{\underline{\theta}}_{1,j}$ are obtained via

$$\hat{\underline{\theta}}_{0,j} = \arg \max_{\underline{\theta}} \prod_{x(n) \in \mathcal{N}_j} f_{0,j}(x(n)) \quad (13)$$

and

$$\hat{\underline{\theta}}_{1,j} = \arg \max_{\underline{\theta}} \prod_{x(n) \in \mathcal{T}_j} f_{1,j}(x(n)) \quad (14)$$

The biases in the parameter estimates, i.e.,

$$E \left[\lim_{j \rightarrow \infty} \arg \max_{\underline{\theta}} \left\{ \prod_{x(n) \in \mathcal{N}_j} (1 - \epsilon)p(x|H_0) + \epsilon p_j^{MD}(x) \right\} \right] - \underline{\theta}_0 \quad (15)$$

and

$$E \left[\lim_{j \rightarrow \infty} \arg \max_{\underline{\theta}} \left\{ \prod_{x(n) \in \mathcal{T}_j} (1 - \epsilon) p_j^{FA} + \epsilon p(x|H_1) \right\} \right] - \underline{\theta}_1 \quad (16)$$

are generally nonzero. Further, the difference between the true and estimated target and noise pdfs, as demonstrated in Equation (12) are generally dependent on the true parameters and thus cannot be corrected for. Except for overly simplified examples, where e.g. $\epsilon = 0$, or where the noise and target pdfs are non-overlapping, the above simple iterative detection approach provides biased parameter estimates and, thus, does not converge to the desired probability of false-alarm, α .

III. THE ITERATIVE ALGORITHM USING MORPHOLOGICAL FILTERING

The values $p_j^{FA}(x)$ and $p_j^{MD}(x)$ distort the estimated pdf's and thus lead to biases in the distribution parameters when applying the iterative detection scheme, we seek methods which eliminate these biases. Since neither the true distribution parameters nor the percentage of targets and noise in a signal are known, an analytical reversal of the bias cannot be achieved. Below, we apply morphological filtering as means to mitigate the errors in the target and noise pdfs [16], [22].

A. Morphological Filtering

When the radar cell size is smaller than the targets spatial extent, target samples would appear in groups forming target objects, whereas noise samples of high intensity will not be necessarily adjacent. In this respect, $p_j^{FA}(x)$, which mistakenly expands the target set \mathcal{T}_j , also truncates the noise set \mathcal{N}_j . This expansion comprises high intensity pixels that are isolated and non-contiguous. On the other hand, $p_j^{MD}(x)$, which truncates \mathcal{T}_j , and at the same time mistakenly expands \mathcal{N}_j comprises grouped contiguous target pixels with low intensity. In radar imaging, the target image intensity decreases from the center of a target object towards its rim [23]. This decreasing depends on the properties of the system point spread function, as high resolution systems lead to sharp images. As such, the samples inherent to $p_j^{MD}(x)$ should be sought at the edges and boundaries of the imaged target.

The above properties are key in the design of the filtering operation as part of the iterative detection approach. Let $b^{FA}(n)$ and $b^{MD}(n)$, $n = 0, \dots, N - 1$ denote the binary signals,

resulting from the false-alarms and missed detections, respectively, as described by $p^{FA}(x)$ and $p^{MD}(x)$. Then, similarly to Equation (12) we can write

$$b^D(n) = b(n) + b^{FA}(n) - b^{MD}(n), \quad n = 0, \dots, N - 1 \quad (17)$$

The filtering operation $\mathcal{V}(\cdot)$ should then satisfy

$$\mathcal{V}(b^D(n)) = b^D(n) - b^{FA}(n) + b^{MD}(n) = b(n), \quad n = 0, \dots, N - 1 \quad (18)$$

The above operation entails removing and adding the binary signals representing false-alarms and missed detections, respectively. We apply morphological filtering [16] for finding both binary signals $b^{FA}(n)$ and $b^{MD}(n)$, $n = 0, \dots, N - 1$. The basic morphological dilation and erosion operations (see e.g. [24], [22]) are used for this purpose. Let \underline{b} , \underline{b}^D , \underline{b}^{FA} and \underline{b}^{MD} be the $N \times 1$ vector representations of $b(n)$, $b^D(n)$, $b^{FA}(n)$ and $b^{MD}(n)$, $n = 0, \dots, N - 1$. Mathematically, the dilation operation can be described by,

$$\underline{b} \oplus E = \{z | [(E^r)_z \cap \underline{b}] \subseteq \underline{b}\}, \quad (19)$$

The variable E is referred to as the structuring element and $(E)_z$ is its translation by point z . The reflection of E , i.e., the part of the signal being covered by the structuring element is denoted by E^r . The variable z marks the origin of the structuring element. The erosion operation between \underline{b} and the structuring element E is defined by all positions of z where the structuring element is completely contained in \underline{b} . Formally,

$$\underline{b} \ominus E = \{z | (E)_z \subseteq \underline{b}\}. \quad (20)$$

In Equations (19) and (20), we applied set operations, viewing each vector as a set of ordered elements. We further define the morphological opening $\underline{b} \circ E$ as an erosion followed by a dilation operation. The basic morphological operations are illustrated in Figure 2, where a structuring element of size 3 is used. In the following, morphological opening is employed to identify and eliminate the distorting signal \underline{b}^{FA} . Hereby, we consider the detected signal \underline{b}^D consisting of a finite number of non-overlapping target and noise objects, i.e.,

$$\underline{b}^D = \sum_{k=1}^K O_k^D, \quad (21)$$

with O_k^D being the k^{th} object in \underline{b}^D and K being the total number of objects in \underline{b}^D . As⁸ indicated by Equation (17), \underline{b}^{FA} consists of all noise samples or objects in \underline{b}^D . Thus, with an adequate structuring element, E_D ,

$$\underline{b}^D \circ E_D = (\underline{b}^D \ominus E_D) \oplus E_D = \sum_{k=1}^K O_k^D \circ E_D = \sum_{k=1}^K (O_k^D \ominus E_D) \oplus E_D \quad (22)$$

$$O_k^D \circ E_D = \emptyset, \forall k \text{ where } |E_D| > |O_k^D| \quad (23)$$

$$O_k^D \circ E_D \approx O_k^D, \forall k \text{ where } |E_D| \leq |O_k^D| \quad (24)$$

$$\underline{b}^{FA} = \sum_{p \in P} O_p^D \text{ with } P := \{k \mid |E_D| > |O_k^D|\} \quad (25)$$

$$\underline{b}^D \circ E_D \approx \underline{b}^D - \underline{b}^{FA} \quad (26)$$

with $|E_D|$ and $|O_k^D|$ being the length of the structuring element and the k -th object, respectively. An example of the application of Equations (22)-(26) is illustrated in Figure 3. We consider a binary signal \underline{b}^D that consists of $K = 6$ objects, three target and three noise objects. By choosing a structuring element as defined by Equation (24), i.e., the one with the size of the smallest target object (in this case $|E_D| = 3$), the morphological opening successfully eliminates all noise objects and leaves all target objects unaltered.

The estimation of the truncating signal \underline{b}^{MD} can be accomplished via a dilation operation with an adequate structuring element E_T . The dilation extends the objects remaining in the signal (ideally only target objects) attempting to encompass the pixels located at the target image boundaries. Formally,

$$\underline{b}^{MD} \approx [(\underline{b}^D - \underline{b}^{FA}) \oplus E_T] - (\underline{b}^D - \underline{b}^{FA}). \quad (27)$$

Therefore,

$$\mathcal{V}(\underline{b}^D) = (\underline{b}^D \circ E_D) \oplus E_T \approx \underline{b}^D - \underline{b}^{FA} + \underline{b}^{MD} \quad (28)$$

as required by Equation (18). The block diagram of the iterative target detector using morphological operations is depicted in Figure 4. It is noted that the difference between Figure 4 and Figure 1 is the inclusion of the morphological filtering after the detection operation.

B. Conditions for Convergence

Having discussed the nominal behavior of the filtering step, the conditions under which $\mathcal{V}(\cdot)$ in combination with the other steps of the iterative algorithm will lead to convergence towards the true distribution parameters should now be examined. We consider a signal $x(n)$, $n = 0, \dots, N - 1$, with N_0 noise samples and N_1 target samples such that $N_0 + N_1 = N$.

In order to determine the conditions of convergence, it is primarily important to know the limitations on the size of the structuring element E_D . The size $|E_D|$, which represents the length of the structuring element for the one-dimensional case, must be determined in consideration of the pixel-allocation error η that is likely to incur. This error is given by,

$$\eta = \alpha^{|E_D|} + \alpha^{|E_D|+1} + \alpha^{|E_D|+2} + \dots \quad (29)$$

where α is the false alarm rate. It is measured by the probability of $|E_D|$, or the relative number of noise samples having an intensity higher than the determined threshold. Given $\alpha \ll 1$, the above expression can be simplified by only considering the largest term in the sum, i.e., $\eta \approx \alpha^{|E_D|}$.

The N_0 noise samples can further be divided into three possible outcomes:

- The number of samples, which correctly have been detected as noise, N_C
- The number of samples, which represent false-alarms with a limited spatial extent of maximum $|E_D| - 1$, denoted as N_F
- The number of samples, which represent false-alarms with a spatial extent larger than or equal to $|E_D|$, which will be referred to as allocation errors, denoted as N_A

Clearly, the equality $N_0 = N_C + N_F + N_A$ holds. The morphological opening with structuring element E_D will successfully eliminate the N_F samples with limited spatial extent, whereas it will fail to remove the N_A allocation errors. Thus, in order to fulfill Equation (23) in one iteration, the total number of allocation errors must be smaller than one. Therefore, we require

$$N_A \leq \eta \cdot (N_0 - |E_D| + 1) \approx \eta \cdot N_0 < 1, \quad (30)$$

with $N_0 - |E_D| + 1$ being the maximum (the targets being located at the edge of the scene) number of locations where a false alarm could occur. For simplification, we invoke the assumption $N_0 \gg (|E_D| - 1)$, which is valid in most images encountered. Accordingly,

we can replace the term $N_0 - |E_D| + 1$ by N_0 , as in (30). The upper constraint on the upper¹⁰ value of E_D is given by,

$$|E_D| \leq \min\{O_k^T\}, \forall k, \quad (31)$$

with O_k^T being the k^{th} target object in \underline{b}^D . This limitation can be deduced from Equation (24). Obviously, missed detection may also lead to the inaptness of the iterative approach to detect all targets. However, as stated above, it can be expected that pixels subject to missed detections appear at the image boundaries of targets. Therefore, it is unlikely that these errors are too significant to compromise the detection of a spatially extended target.

Denote β as the true sample threshold resulting from Neyman-Pearson, given exact knowledge of the distribution functions under the null and alternative hypothesis. Then, for an initial threshold $\beta_0 < \beta$, associated with the initial parameters $\hat{\underline{\theta}}_{0,0}, \hat{\underline{\theta}}_{1,0}$, convergence will occur, by definition, if more noise samples are eliminated by the operator $\mathcal{V}(\cdot)$ than when the initial threshold assumes the correct value β . If α_0 is the false alarm rate resulting from a low threshold β_0 , then the new allocation error η_0 becomes

$$\eta_0 = \alpha_0^{|E_D|} + \alpha_0^{|E_D|+1} + \alpha_0^{|E_D|+2} + \dots \quad (32)$$

It follows from Equation (29) that, for the same $|E_D|$, $\eta_0 > \eta$, since $\alpha_0 > \alpha$ for $\beta_0 < \beta$.

With $\eta_0 > \eta$, the filtering operation will not always yield a convergence towards the true parameters in all cases, since it is conceivable that allocation errors persist through the iterative scheme. Three possible cases can be identified:

- 1) The number of errors N_A is zero. Thus, all noise samples are successfully removed and the true parameters can be estimated from the resulting sets. In this case, the number of false-alarms is reduced from N_F to 0 and convergence occurs after the first iteration.
- 2) Allocation errors occur, but N_A is smaller than the number of false alarms with a limited spatial extent, i.e., $N_A < N_F$. In this case, the operation $\mathcal{V}(\cdot)$ will yield an improvement of the estimated distribution parameters, but not the true parameters, as the number of false-alarms is reduced from $N_A + N_F$ to N_A . Further iterations will be needed until convergence towards the true parameters occurs. The new threshold β_1 will be higher than or equal to β_0 , thus yielding a new false alarm rate α_1 with $\alpha \leq \alpha_1 \leq \alpha_0$.
- 3) In the case $N_A > N_F$ convergence towards the true parameters will generally not occur.

Under this condition, the new parameters will result in a new threshold $\beta_1 \leq \beta_0$, which¹¹ will elicit even more allocation errors $\eta_1 \geq \eta_0$ until all noise is potentially classified as a target.

For the case that $\beta_0 > \beta$, similar conclusions to those discussed above can be drawn. In this case a false-alarm rate α_0 that is lower than the preset α is obtained, possibly leading to allocation errors in the target set. As shown above, again three cases can be considered

- No target allocation errors occur. In this case, the morphological dilation via E_T will restore the target signal in one iteration.
- Target allocation errors occur, but their number is smaller than the number of unaffected target samples. In this case, a new iteration yields $\beta_1 \leq \beta_0$ and thus $\alpha \geq \alpha_1 > \alpha_0$
- More target allocation errors occur than the number of unaffected target samples. In this case, convergence towards the true parameters generally will not occur. The new threshold β_1 will be even higher than β_0 , yielding $\alpha_1 < \alpha_0$. Thus, further iterations will eliminate target objects, until all targets are potentially classified as being noise.

The practical implication of this section is that the initial parameters of the iterative algorithm should be chosen pessimistically, but not exceedingly pessimistic, since this could lead to the third case described above. Details on how initial parameters, or, equivalently, an initial binary signal can be chosen will be provided in Section VI.

IV. OPTIMIZING THE STRUCTURING ELEMENT

As shown in the previous Section, the expected number of pixel-allocation errors ($\approx N_0 \cdot \eta$) in the processed signal is dependent on the size and, in the case of two or three dimensional images, shape of the structuring elements. A structuring element of the same size and shape as the smallest target object will minimize the expected errors, thus rendering the best possible estimation of the parameters under the null and alternative hypothesis. Unfortunately, it is not always valid to presume any a priori knowledge of the size and shape of target objects in the scene of interest. For this reason, a method for finding the correct structuring elements is vital for the success of the iterative detection approach.

In [16], we have suggested that the detection of non-comprehensive estimates for \underline{b}^{FA} and \underline{b}^{MD} can be used for the purpose of finding an appropriate structuring element. The

employment of a non-ideal structuring element \tilde{E}_D will by definition lead to truncated and/or¹² distorted target and noise data sets $\tilde{\mathcal{T}}$ and $\tilde{\mathcal{N}}$ respectively.

Here, we propose to detect such corrupted sets via a comparison of parametric and non-parametric density estimators. We compare a parametric model, e.g., $p(x|H_0; \hat{\underline{\theta}}_{0,J})$ and a non-parametric model $f_{0,J}(x)$, where the index J stands for the J -th, i.e., final iteration. This comparison, which can be based on the MSE, is suitable for detecting non-comprehensive estimates for \underline{b}^{FA} and \underline{b}^{MD} , if the following inequality holds true (the noise set is considered exemplarily):

$$\mathbb{E} [(f_0(x) - p(x|H_0; \underline{\theta}_0))^2] < \mathbb{E} [(\tilde{f}_{0,J}(x) - p(x|H_0; \hat{\underline{\theta}}_{0,J}))^2] \quad (33)$$

Here, $f_0(x)$ denotes a non-parametric estimate of the noise pdf and $p(x|H_0; \underline{\theta}_0)$ denotes the parametric density under the null hypothesis, given the true parameters $\underline{\theta}_0$. $f_{0,J}(x)$ is a non-parametric density estimation of the noise at the J -th, i.e., final iteration, as detailed in Equation (5), whereas $p(x|H_0; \hat{\underline{\theta}}_{0,J})$ is the parametric density under the null hypothesis given the parameter estimates from the J -th iteration step. The non-parametric density estimator has to be chosen in accordance with the postulated inequality of Equation (33). In this light, we suggest the employment of a kernel density estimator [25] as

$$f_0(x) = \frac{1}{hN} \sum_{n=0}^{N-1} K\left(\frac{x - x^{(n)}}{h}\right) \quad (34)$$

with $K(\cdot)$ and h being the kernel function and bandwidth, respectively. By definition, $p(x|H_0; \underline{\theta}_0)$ describes the true distribution of \mathcal{N} with the true set of distribution parameters $\underline{\theta}_0$. The expected value of $f_0(x)$ being

$$\mathbb{E} [f_0(x)] = \int_{-\infty}^{\infty} \frac{1}{h} K\left(\frac{x - y}{h}\right) p(y|H_0; \underline{\theta}_0) dy = p(x|H_0; \underline{\theta}_0) \quad (35)$$

and

$$\lim_{N \rightarrow \infty} Nh \cdot \text{Var}[f_0(x)] = p(x|H_0; \underline{\theta}_0) \int_{-\infty}^{\infty} K^2(y) dy \quad (36)$$

Proof and conditions for Equations (35) and (36) are presented in [26]. The MSE is thus

lower bounded by the left side of Equation (33), since

$$\lim_{N \rightarrow \infty} \mathbb{E} \left[(f_0(x) - p(x|H_0; \underline{\theta}_0))^2 \right] = 0 \quad (37)$$

It remains to show, that the MSE for any $\tilde{f}_{0,J}(x)$ resulting from the set \mathcal{N}_J is asymptotically greater than zero. The non-parametric distribution model of the underlying data \mathcal{N}_J can be expressed as follows

$$\begin{aligned} \tilde{f}_{0,J}(x) = \frac{N}{N + N_J^{FA} - N_J^{MD}} & \left[f_0(x) + \frac{1}{hN} \sum_{\{n|b_J^{FA}(n)=1\}} K \left(\frac{x - b_J^{FA}(n)}{h} \right) \right. \\ & \left. - \frac{1}{hN} \sum_{\{n|b_J^{MD}(n)=1\}} K \left(\frac{x - b_J^{MD}(i)}{h} \right) \right], \end{aligned} \quad (38)$$

with N_J^{FA} and N_J^{MD} being the number of detected samples in $b_J^{FA}(n)$ and $b_J^{MD}(n)$, $n = 0, \dots, N-1$ respectively. Considering Equation (35), the expected value of Equation (38) can be written as

$$\mathbb{E}[\tilde{f}_{0,J}(x)] = a_1 p(x|H_0; \underline{\theta}_0) + a_2 f_{FA}(x) - a_3 f_{MD}(x), \quad (39)$$

with a_1, \dots, a_3 being scaling factors and $f_{FA}(x)$ and $f_{MD}(x)$ being the distribution functions of the remaining distorting and truncating sets. As per definition, $f_{FA}(x)$ has no impact below the respective threshold β_J and on the other hand, $f_{MD}(x)$ has no impact above β_J , the case that

$$a_2 f_{FA}(x) - a_3 f_{MD}(x) \sim p(x|H_0; \underline{\theta}_0) \quad (40)$$

can practically be excluded. In any other case, there will exist a Bias $[\tilde{f}_{0,J}(x)] = \mathbb{E}[\tilde{f}_{0,J}(x)] - p(x|H_0; \hat{\underline{\theta}}_{0,J})$ greater than zero and therefore

$$\lim_{N \rightarrow \infty} \mathbb{E} \left[(\tilde{f}_{0,J}(x) - p(x|H_0; \hat{\underline{\theta}}_{0,J}))^2 \right] > 0 \quad (41)$$

With the validity of Equation (33) shown, the structuring element may be optimized by repeating the iterative detection procedure with structuring elements E_D^s , $s = 1, \dots, S$, and

then choosing

$$\hat{E}_D = \arg \min_{E_D^s} G \left(\text{MSE} \left[\tilde{f}_{1,J}(x), p(x|H_1; \hat{\theta}_{1,J}) \right], \text{MSE} \left[\tilde{f}_{0,J}(x), p(x|H_0; \hat{\theta}_{0,J}) \right] \mid E_D^s \right), \quad (42)$$

with $G(\cdot)$ being a function merging the mean squared errors computed for the iteratively estimated target and noise densities. The exact technique of merging the MSEs can be chosen according to the measure of confidence regarding the validity of the noise and target density class models, respectively. If, for example, one is fairly confident that noise stems from a Gaussian distribution, but less confident about the target density class, then it is advisable to design a function $G(\cdot)$, which assigns a greater weight to the MSE resulting from the noise models. Furthermore, because its variation is not confined to individual pixels it may be of advantage to vary the false alarm rate α instead of the structuring element E_D as suggested by Equation (42). For the one-dimensional case the relation between the two is expressed in Equation (29).

V. SIMULATION RESULTS

In order to assess the performance of the proposed methods, namely,

- The simple iterative detection approach (without filtering step)
- The iterative detection approach using morphological filtering (static structuring element)
- The iterative detection approach using an adaptive morphological filtering

we consider a three-dimensional scene description, as depicted in Figure 5. The signal is composed of three nonoverlapping square-sized target objects following a Gaussian distribution and noise following a Weibull densities being present in the remaining scene. Gaussian (target) and Weibull (noise) have been chosen to mimic 3D TWRI images which have empirically been shown [10] to follow these distributions. We note that the assumption in Section II that the likelihood ratio threshold γ_0 corresponds to a single sample threshold β_0 is not valid when considering a Gaussian and Weibull density for modelling the two hypotheses. It is thus considered as an approximation in the following.

The iterative detection approach can easily be extended to 3D images by separating a 3D image into a set of 2D images where two-dimensional morphological operations can be used. Given the TWRI application in mind, this would correspond to a separate treatment of each radar B-Scan.

The improvement of the parameter estimates with the number of iterations using the iterative¹⁵ detection approach without and with morphological filtering is delineated. The parameters of the distributions under the null and alternative hypotheses are:

$$\underline{\theta}_0 = \begin{pmatrix} \kappa_0 \\ \lambda_0 \end{pmatrix} = \begin{pmatrix} 1 \\ 2.5 \end{pmatrix}; \quad \underline{\theta}_1 = \begin{pmatrix} \mu_1 \\ \sigma_1 \end{pmatrix} = \begin{pmatrix} 10 \\ 0.5 \end{pmatrix} \quad (43)$$

where κ_0 and λ_0 denote the scale and shape parameter of the Weibull distribution, respectively. Figure 6 (a)-(d) shows the development of the parameter estimates $\hat{\kappa}_0, \hat{\mu}_1, \hat{\lambda}_0, \hat{\sigma}_1$ for $j = 1, \dots, 20$ iterations of the proposed detectors using the Neyman-Pearson test for detection with a false-alarm rate of $\alpha = 0.05$. The results were obtained using 1000 Monte Carlo simulations. The parameter estimates shown at the 0th iteration correspond to the initially chosen parameters and are identical for both methods. The structuring element is of length $|E_D| = 10$.

As evident from Figure 6 (a)-(d), a considerable bias is visible when choosing the iterative target detector without morphological filtering. This bias, which has been derived in Section II (Equations (15) and (16)), is caused by the inability to recover the pdf's under H_0 and H_1 without an additional filtering operation. Bias in the parameter estimates will ultimately lead to a detector which does not provide the required false-alarm rate. On the other hand, the iterative detector using morphological filtering quickly converges towards the true parameters (in this simple example, convergence after $J = 3 - 4$ iterations is achieved).

The choice of an optimal structuring element, as proposed in Section IV, becomes crucial when varying statistics are considered. We therefore consider a similar scenario as above, except that κ_0 is varied between 0 and 20. As a performance measure, the mean absolute deviation (MAD) of the obtained binary signal \underline{b}_J^D after J iterations and the true binary signal \underline{b} is used as

$$\text{MAD}(\underline{b}_J^D, \underline{b}) = \frac{1}{N} \sum_n |b_J^D(n) - b(n)| \quad (44)$$

where a vectorized notation of the 3D image is used for simplicity. The MAD using the scenario described above is depicted in Figure 7. It can be observed, that the proposed detector without filtering operation (dotted line) has a constant error, even for small κ_0 . This corresponds to the bias in the parameter estimates described above. The iterative detector

with a static structuring element $|E_D| = 10 \times 10$ (dashed line) shows an improvement,¹⁶ but has an early breakdown point at $\kappa_0 \approx 6$, where the chosen, static structuring element is no longer able to separate target and noise data. The same statement holds when choosing a static 10×10 median filter as in [10] (solid line). Here, the detector already breaks down at $\kappa_0 \approx 5$. When using an optimized structuring element (solid line with dotted markers), as proposed by Equation (42) (in our example, $G(\cdot)$ is just a simple averaging operation), we can accept a far higher noise level, $\kappa \approx 8$. Beyond the breakdown point, we observe occurrence of the scenario which was analytically derived in Section III-B. In this case, the allocation error is so large that convergence towards the true parameters cannot be achieved and either all samples are classified as being noise or target exclusively. It is further noted that in high SNR, the adaptive approach does not yield improvement over the static approach. This is due to the fact that for a small κ_0 , only few false alarms will occur which are likely to be isolated. Thus, any reasonably chosen structuring element of size $|E_D| > 1 \times 1$ will perform equally well in the elimination of these outliers and an adaptive structuring element size will not enhance the detector performance.

We further demonstrate the performance of the two-parameter OSCFAR detector (dash-dotted line), derived in [15]. As proposed by Rohling [12] the 75th percentile has been used to obtain the image threshold. The OSCFAR detector shows a continuous degradation as opposed to the breakdown-point behavior of the iterative approach. However, for most scenarios it also shows a worse performance in terms of MAD.

We note that the choice of the structuring element E_T used to restore missed detections is more problematic. The optimal configuration depends on the target characteristic and system point spread function. A square static structuring element of size 3×3 is chosen which effectively enlarges each remaining target object by one pixel. It shall, however, be noted that one could consider a joint optimization of E_D and E_T which will be a subject of future research.

VI. EXPERIMENTAL RESULTS

In this Section, the proposed detectors are applied for the detection of stationary targets in Through-the-Wall Radar Imaging (TWRI) applications. We consider an experimental setup depicted in Figure 8. Three metallic objects (sphere, dihedral and trihedral) are placed on

high foam columns at different heights behind a solid concrete block wall. The respective dimensions are shown in Figure 9. The wall parameters are $d = 5.625in$ (wall thickness) and $\varepsilon = 7.66$ (dielectric constant). For imaging, a 57×57 element planar array with an interelement spacing of $0.875in$ was used, which has been synthesized using a single horn antenna. The array is centered at a height of $48in$ above ground. The scene is illuminated using a stepped-frequency continuous-wave (CW) signal with a bandwidth of 2.4 GHz and a center frequency of 1.9 GHz, where 801 frequencies with a stepsize of 3 MHz are used. We note that the following conclusions are drawn based on an extensive study performed on several data sets, but these cannot be reproduced due to space limitations.

There exist many approaches for the actual beamforming or image formation process. This includes tomographic approaches [27], [28], [29] where the image formation is seen as an inverse scattering problem and differential SAR [30]. In this paper we restrict ourselves to wideband delay and sum beamforming [31], [32], although we maintain that the proposed detectors are postprocessing methods and as such are independent of the actual imaging process.

We consider known wall parameters for beamforming. References [33], [34], [11] describe methods on how to estimate unknown wall parameters.

For beamforming, we consider two possible schemes for removal of signal reflections from walls.

- **Background-Subtraction:** In this case, we assume that empty scene measurements are available. The received signal amplitudes obtained when illuminating the empty scene can thus be coherently subtracted from the signal amplitudes obtained when illuminating the filled scene.
- **Wall Removal:** In practice, empty scene measurements are often not available. We follow the simple approach from [35] where a spatial notch filter is used to remove wall effects. The spatial filter used is given by

$$H(e^{j\omega}) = \frac{1 - e^{-j\omega}}{1 - \varrho e^{-j\omega}} \quad (45)$$

where a notch width $\varrho = 0.8$ is chosen. Further, as proposed in [35], two-way filtering and downsampling of the antenna outputs by a factor of 2 is implemented.

Typical B-Scans (2D images at particular heights of interest) resulting from the wideband¹⁸ beamformer using raw data, background subtraction and wall removal are shown in Figures 10(a)-(f). Two different heights are considered, namely, -5 in and $+25$ with respect to the array center. Here, the objects of interest are marked by solid (triangular), dashed (dihedral) and dotted (sphere) circles. Clearly, the images in Figure 10(a) and (b) obtained from the raw data without preprocessing to remove the wall reflections are very cluttered and cannot be used for detection. With background subtraction preprocessing of the data, the image at lower heights, e.g. at -5 in, has high clutter at approx. $-2, \dots, -6$ ft crossrange and $8, \dots, 12$ ft downrange (see Figure 10(c)). Also, as the objects in the scene are placed at different heights, they may only be visible at specific B-Scans, as evident from Figure 10(d). The dihedral has a large radar cross-section and was visible in practically all B-Scans from $-10, \dots, +30$ in. The metal sphere and the triangular, on the other hand have a rather small radar cross-section and are only visible within a small range of B-Scans. When using the simple spatial filter based wall removal technique, a large increase in clutter can be observed as shown in Figures 10(e) and (f). It shall be noted that the clutter is comparable to or even stronger than the targets which will affect subsequent detection results.

The proposed detector, derived for 1D signals, can easily be extended to 2D signals by choosing two-dimensional structuring elements for morphological filtering and applying pixelwise detection, as detailed in e.g. [10], [16]. By applying the detector to a set of B-Scans obtained at different heights, finally a 3D binary representation of the scene can be obtained.

As shown in [10], [16], the usage of a Weibull distribution for $p(x|H_0)$ and a Gaussian pdf for $p(x|H_1)$ are appropriate choices when considering the above mentioned setup for TWRI. Again, the Neyman-Pearson test has been used as a detector, where the likelihood ratio threshold is obtained by integrating over the pdf of the likelihood ratio under the null hypothesis, per Equation (3). For initialization, instead of using initial parameter vectors $\hat{\theta}_0$ and $\hat{\theta}_1$, which may be difficult to discern in practice, we propose using an initial binary image instead, which is easier to obtain. We choose the initial binary image $B_0^D(n, m)$, $n = 0, \dots, N - 1$, $m = 0, \dots, M - 1$ as

$$B_0^D(n, m) = \begin{cases} 1, & X(n, m) > \text{med}(X) \\ 0, & X(n, m) \leq \text{med}(X) \end{cases} \quad (46)$$

where $X(n, m)$, $n = 0, \dots, N-1$, $m = 0, \dots, M-1$ is the B-Scan under detection and $\text{med}(X)$ ¹⁹ is the median image value. Thus it is guaranteed that in the first iteration, half of the image values are assigned to the target set \mathcal{T}_0 and the other half to the noise set \mathcal{N}_0 . This simplified the estimation of the initial (truncated and distorted) target and noise distributions.

The 3D detection result using the iterative detector with a static structuring element of size 3×3 is shown in Figure 11(a) for background-subtracted images. A false-alarm rate of 1% has been chosen. It is evident that the chosen structuring element is suboptimal. Although the circle (dotted ellipse) and the trihedral (solid ellipse) can be detected, the dihedral (dashed ellipse) can hardly be separated from the large amount of clutter present in the respective image region.

For the iterative detector using adaptive morphological filtering we chose the optimization procedure as presented in Section IV, whereby we restricted ourselves to quadratic structuring elements for simplicity. The corresponding 3D detection result (again, using background-subtracted data) is shown in Figure 11(b). Now, all three objects can clearly be detected and the amount of clutter is strongly reduced to a small volume at approx. 8, ..., 10 ft. downrange and $-5, \dots, -3$ ft. crossrange. The iterative detector adapts itself to the image statistics which are varying within the scene. This is demonstrated by plotting in Figure 12 the noise statistics (shape and scale parameter of the Weibull distribution), the chosen structuring element size and the output of the goodness-of-fit (GOF) function (Equation (42)) for all heights $-10, \dots, +30$ in. It is clear that the structuring element automatically varies between 4×4 and 7×7 . The noise is stronger in the upper and lower region of the 3D scene and is also varying its shape (Note that a shape parameter of 2 corresponds to a Rayleigh distribution which would not be an appropriate choice here). Further, it shall be noted that in the middle region of the 3D scene the GOF function yields relatively large values which implies that the assumed models for target and noise distributions are suboptimal. Improvements could be obtained using resampling schemes such as the bootstrap [36] which may turn out especially useful for small data sizes.

The 3D detection result when using the OSCFAR detector is depicted in Figure 13 for comparison. Trihedral and sphere can clearly be detected, however it is hard to discriminate the dihedral from its surrounding. Further, a strong amount of clutter at approx. 8, ..., 10 ft.

downrange and $-5, \dots -3$ ft. crossrange deteriorates the detection.

The 3D detection result when using the wall removal procedure from [35] is depicted in Figure 14(a) and (b). As expected by the strong amount of clutter left in the radar images (Figures 10(e) and (f)), detection becomes much harder when secondary data for background-subtraction is not available. This holds for the proposed detector as well as for the OSCFAR detector. The metal sphere, which has a relatively small radar cross section is no longer visible. The dihedral and trihedral can still be detected, but are embedded in strong clutter. We note that wall reflection removal methods which estimate the wall parameters and proceed to model wall EM returns and subtract them from the data can lead to better removal of clutter [8], [37] compared to spatial filtering which does not require estimation of the wall EM characteristics. We maintain, however, that the proposed detection scheme is a postprocessing operation which can be applied with any wall EM removal techniques.

The computational complexity of the proposed approaches is determined by the number of iterations J and structuring elements S . As the computation time for one iteration is comparable to that of the OSCFAR, the proposed approach increases in complexity by a factor of $J \cdot S$, which would typically be around $3 - 5$ when using static morphological filtering, and approx. $20 - 30$ when using the adaptive morphological filtering.

VII. CONCLUSION

An iterative target detector has been presented which adapts itself to different and unknown image statistics. We have shown that there is need for an additional morphological filtering step to reduce the bias in parameter estimation, which typically occurs when using a simple version of the detector. Properties of the proposed detector such as conditions for convergence, optimal choices of the structuring element for morphological filtering and practical issues such as the choice of initial parameters were examined. The proposed detector was applied to synthetic 1D data to demonstrate its performance. It was applied for target detection in Through-the-Wall radar imaging, where the image statistics vary with space. Background-subtraction as well as a wall removal method based on a spatial notch filter have been investigated. When using the proposed iterative detector with an optimum choice of the structuring element, targets in the case of background-subtracted images have been clearly detected which enhances subsequent steps such as feature extraction or classification of targets. When considering simple wall

removal techniques without knowledge of the background, a strong amount of false alarms²¹ deteriorates the detection results.

ACKNOWLEDGEMENT

The authors would like to thank Dr. Fauzia Ahmad, the director of the Radar Imaging Lab at Villanova University, Villanova, PA, USA, for providing the experimental data.

REFERENCES

- [1] D. Massonnet and J.-C. Souyris, *Imaging with Synthetic Aperture Radar*, CRC Press, 2008.
- [2] R.J. Sullivan, *Microwave Radar Imaging and Advanced Concepts*, Artech House Inc, 2000.
- [3] M. Amin and K. Sarabandi (Guest Editors), “Special issue on remote sensing of building interior,” *IEEE Transactions on Geoscience and Remote Sensing*, vol. 47, no. 5, 2009.
- [4] M. Amin (Guest Editor), “Special issue: Advances in indoor radar imaging,” *Journal of the Franklin Institute*, vol. 345, no. 6, 2008.
- [5] E. Baranoski and F. Ahmad (Session Chairs), “Special session on through-the-wall radar imaging,” in *IEEE International Conference on Acoustics, Speech and Signal Processing*, 2008.
- [6] E. Baranoski, “Through-wall imaging: Historical perspective and future directions,” *Journal of the Franklin Institute*, vol. 345, no. 6, pp. 556–569, 2008.
- [7] F. Ahmad and M. G. Amin, “Through-the-wall radar imaging experiments,” in *IEEE Workshop on Signal Processing Applications for Public Security and Forensics*, Moeness G. Amin, Ed., 2007, pp. 1–5.
- [8] M. Dehmollaian and K. Sarabandi, “Refocusing through building walls using synthetic aperture radar,” *IEEE Transactions on Geoscience and Remote Sensing*, vol. 46, no. 6, pp. 1589–1599, 2008.
- [9] A. Muqaibel, A. Safaai-Jazi, A. Bayram, M. Attiya, and S.M. Riad, “Ultrawideband through-the-wall propagation,” *IEE Proceedings Microwave, Antennas and Propagation*, vol. 152, pp. 581–588, 2005.
- [10] C. Debes, M.G. Amin, and A.M. Zoubir, “Target detection in single- and multiple-view through-the-wall radar imaging,” *IEEE Transactions on Geoscience and Remote Sensing*, vol. 47(5), pp. 1349 – 1361, 2009.
- [11] G. Wang and M.G. Amin, “Imaging through unknown walls using different standoff distances,” *IEEE Transactions on Signal Processing*, vol. 54, no. 10, pp. 4015–4025, Oct 2006.
- [12] H. Rohling, “Radar CFAR thresholding in clutter and multiple target situations,” *IEEE Transactions on Aerospace and Electronic Systems*, vol. 19, no. 4, pp. 608–621, 1983.
- [13] M. di Bisceglie and C. Galdi, “CFAR detection of extended objects in high-resolution SAR images,” *IEEE Transactions on Geoscience and Remote Sensing*, vol. 43, no. 4, pp. 833–843, 2005.
- [14] M. Weiss, “Analysis of some modified cell-averaging CFAR processors in multiple-target situations,” *IEEE Transactions on Aerospace and Electronic Systems*, vol. 18, no. 1, pp. 102–114, 1982.
- [15] P. Weber and S. Haykin, “Ordered statistic CFAR processing for two-parameter distributions with variable skewness,” *IEEE Transactions on Aerospace and Electronic Systems*, vol. 21, no. 6, pp. 819–821, 1985.
- [16] C. Debes, J. Riedler, M.G. Amin, and A.M. Zoubir, “Iterative target detection approach for through-the-wall radar imaging,” in *Proceedings of the IEEE International Conference on Acoustics, Speech and Signal Processing*, 2009, pp. 3061 – 3064.
- [17] N. Maaref, P. Millot, P. Pichot, and O. Picon, “A study of UWB FM-CW radar for the detection of human beings in motion inside a building,” *IEEE Transactions on Geoscience and Remote Sensing*, vol. 47, no. 5, pp. 1297–1300, 2009.
- [18] Y. Kim and H. Ling, “Human activity classification based on micro-doppler signatures using a support vector machine,” *IEEE Transactions on Geoscience and Remote Sensing*, vol. 47, no. 5, pp. 1328–1337, 2009.
- [19] A. Lin and H. Ling, “Through-wall measurements of a doppler and direction-of-arrival (DDOA) radar for tracking indoor movers,” in *Proceedings of the IEEE Antennas and Propagation Society*, 2005, vol. 3B, pp. 322–325.
- [20] S.M. Kay, *Fundamentals of Statistical Signal Processing, Volume 2: Detection Theory*, Prentice Hall, 1998.

- [21] S.M. Kay, *Fundamentals of Statistical Signal Processing, Volume 1: Estimation Theory*, Prentice Hall, 1993.
- [22] R. Stevenson and G. Arce, "Morphological filters: Statistics and further syntactic properties," *IEEE Transactions on Circuits and Systems*, vol. 34, no. 11, pp. 1292–1305, 1987.
- [23] F.T. Ulaby, F. Kouyate, B. Brisco, and T.H.L. Williams, "Textural information in SAR images," *IEEE Transactions on Geoscience and Remote Sensing*, vol. GE-24, no. 2, pp. 235–245, 1986.
- [24] R.C. Gonzales and R.E. Woods, *Digital Image Processing*, Prentice Hall, 2001.
- [25] B. Silverman, *Density Estimation for Statistics and Data Analysis*, Chapman & Hall, 1986.
- [26] E. Parzen, "On estimation of a probability density function and mode," *Annals of Mathematical Statistics*, vol. 33, pp. 1065–1076, 1962.
- [27] F. Soldovieri and R. Solimene, "Through-wall imaging via a linear inverse scattering algorithm," *IEEE Geoscience and Remote Sensing Letters*, vol. 4, pp. 513–517, 2007.
- [28] L.-P. Song, C. Yu, and Q. H. Liu, "Through-wall imaging (twi) by radar: 2-D tomographic results and analyses," *IEEE Transactions on Geoscience and Remote Sensing*, vol. 43, no. 12, pp. 2793–2798, 2005.
- [29] R. Solimene, F. Soldovieri, G. Prisco, and R. Pierri, "Three-dimensional microwave tomography by a 2-d slice-based reconstruction algorithm," *IEEE Geoscience and Remote Sensing Letters*, vol. 4, no. 4, pp. 556–560, 2007.
- [30] M. Dehmollaian, M. Thiel, and K. Sarabandi, "Through-the-wall imaging using differential SAR," *IEEE Transactions on Geoscience and Remote Sensing*, vol. 47, no. 5, pp. 1289–1296, 2009.
- [31] F. Ahmad and M.G. Amin, "Multi-location wideband synthetic aperture imaging for urban sensing applications," *Journal of the Franklin Institute*, vol. 345, no. 6, pp. 618–639, 2008.
- [32] F. Ahmad, Y. Zhang, and M.G. Amin, "Three-dimensional wideband beamforming for imaging through a single wall," *IEEE Geoscience and Remote Sensing Letters*, vol. 5, no. 2, pp. 176–179, 2008.
- [33] R. Solimene, F. Soldovieri, G. Prisco, and R. Pierri, "Three-dimensional through-wall imaging under ambiguous wall parameters," *IEEE Transactions on Geoscience and Remote Sensing*, vol. 47, no. 5, pp. 1310–1317, 2009.
- [34] L. Li, W. Zhang, and F. Li, "A novel autofocus approach for real-time through-wall imaging under unknown wall characteristics," *IEEE Transactions on Geoscience and Remote Sensing*, vol. 48, no. 1, pp. 423–431, 2010.
- [35] Y.-S. Yoon and M. G. Amin, "Spatial filtering for wall-clutter mitigation in through-the-wall radar imaging," *IEEE Transactions on Geoscience and Remote Sensing*, vol. 47, no. 9, pp. 3192–3208, 2009.
- [36] A.M. Zoubir and D. R. Iskander, *Bootstrap Techniques for Signal Processing*, Cambridge University Press, 2004.
- [37] M. Dehmollaian and K. Sarabandi, "Analytical, numerical, and experimental methods for through-the-wall radar imaging," in *IEEE International Conference on Acoustics, Speech and Signal Processing*, 2008, pp. 5181–5184.

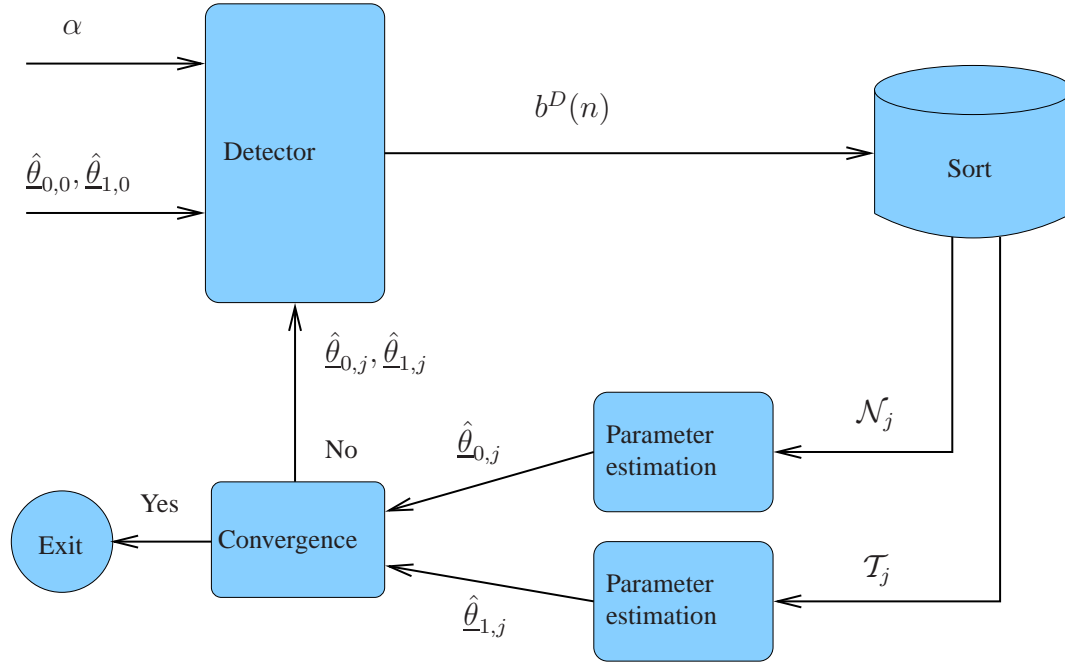


Fig. 1. Block diagram representation of the simple iterative detection approach

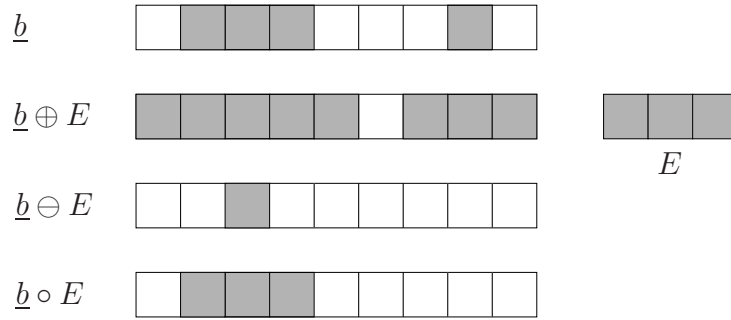


Fig. 2. Basic morphological operations

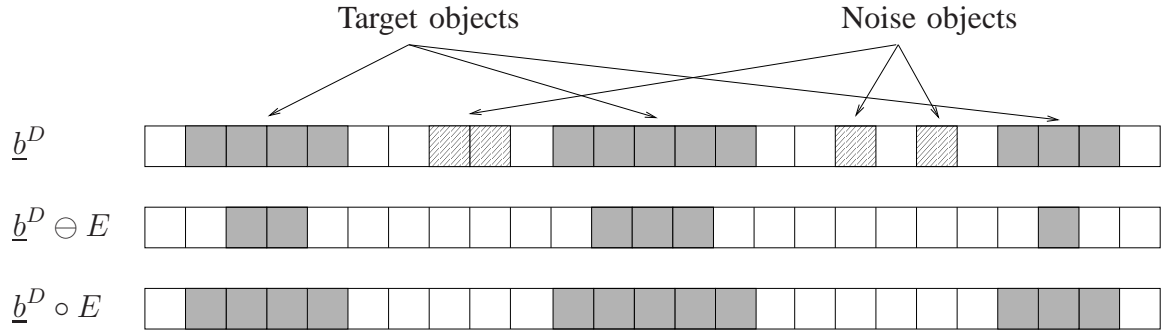


Fig. 3. Choosing the adequate structuring element

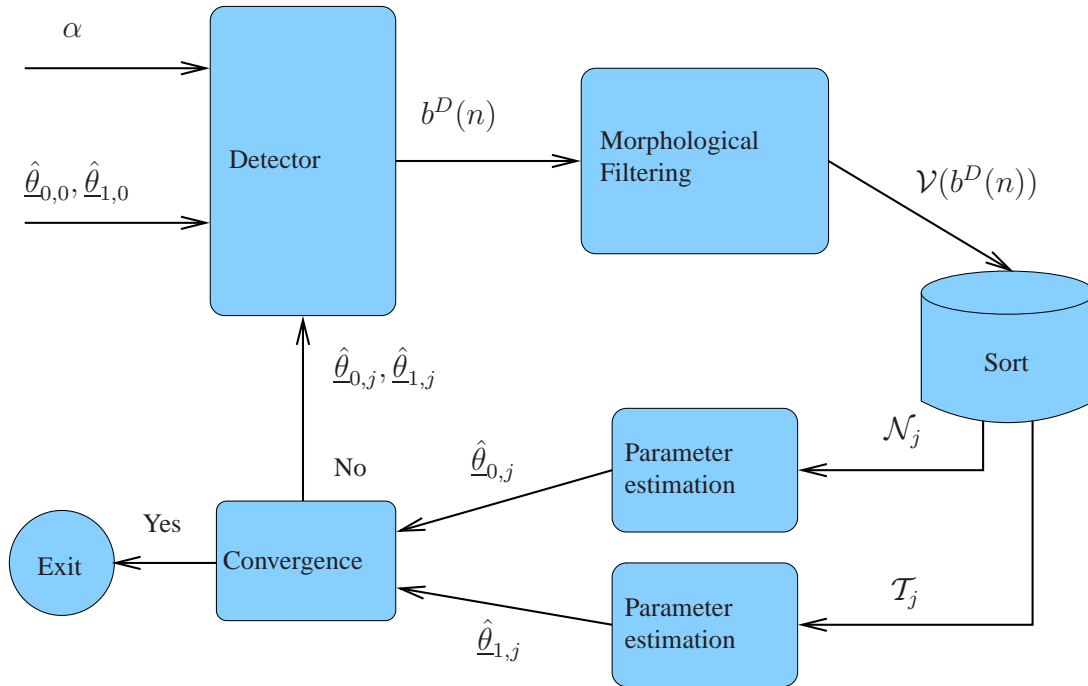


Fig. 4. Block diagram representation of the iterative detection approach using morphological filtering

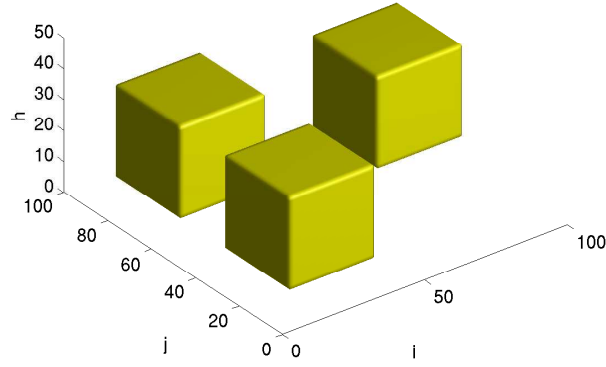


Fig. 5. Synthetic 3D signal

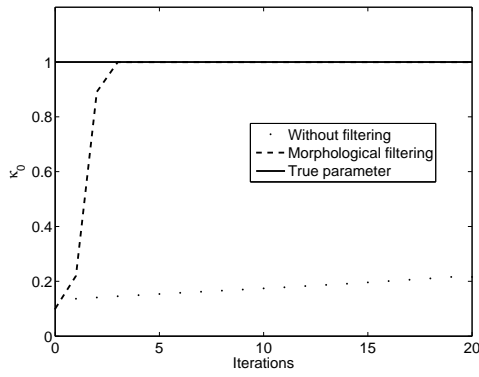
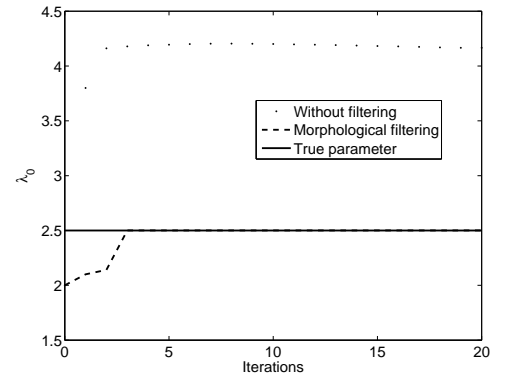
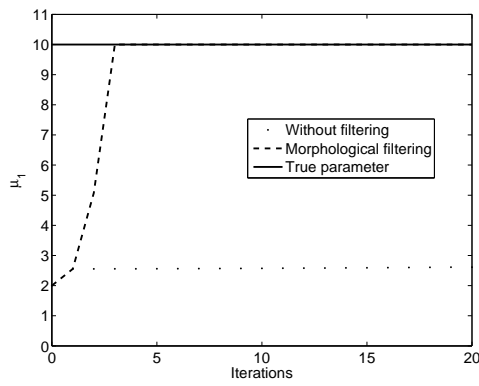
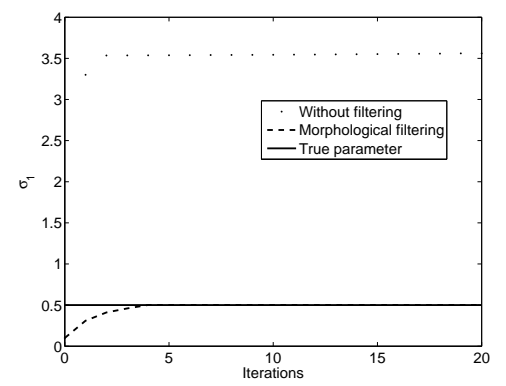
(a) Estimating κ_0 (b) Estimating λ_0 (c) Estimating μ_1 (d) Estimating σ_1

Fig. 6. Parameter estimation improvement using the iterative detection approach

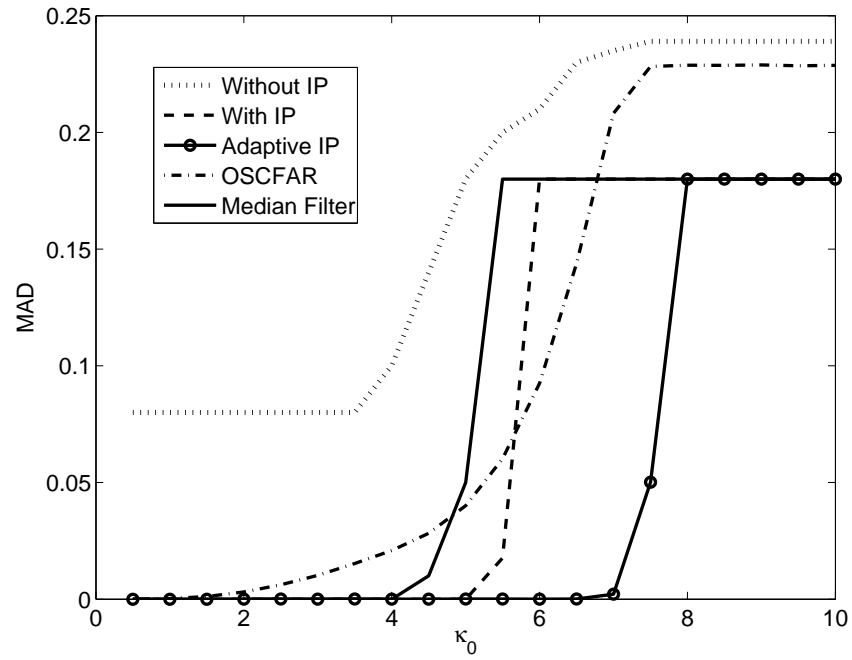


Fig. 7. Performance gain when using an adaptive image processing step



Fig. 8. Scene of interest

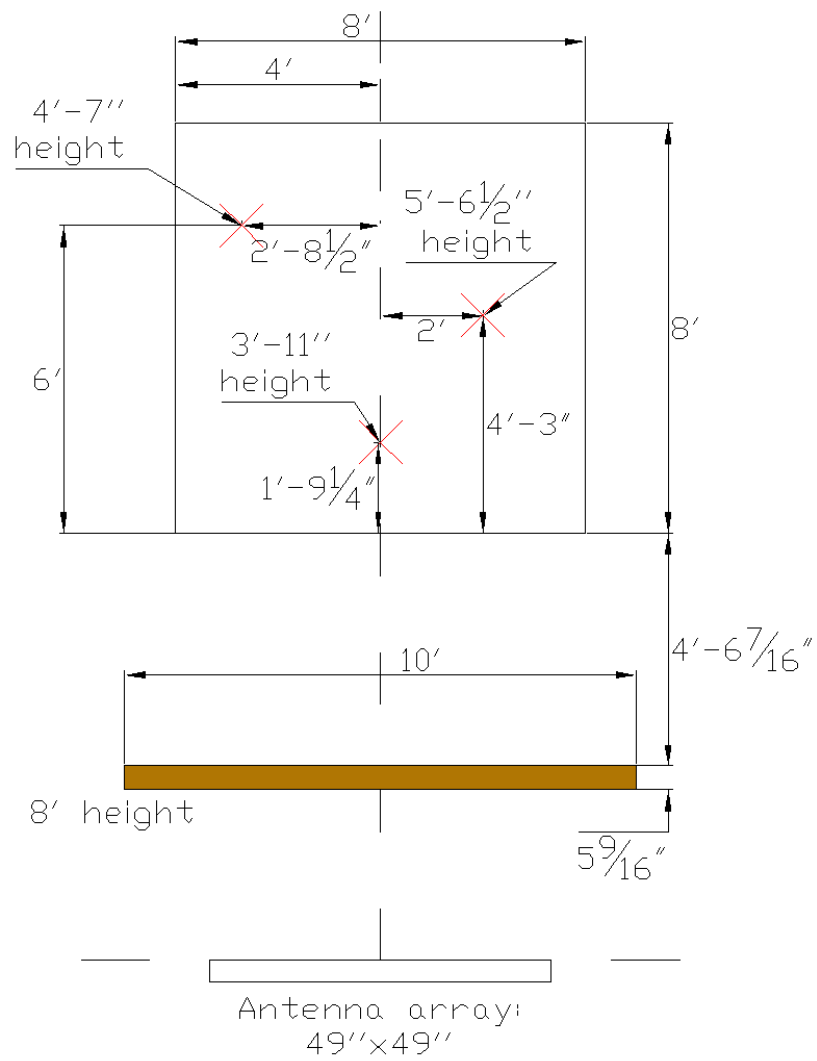


Fig. 9. Scene layout

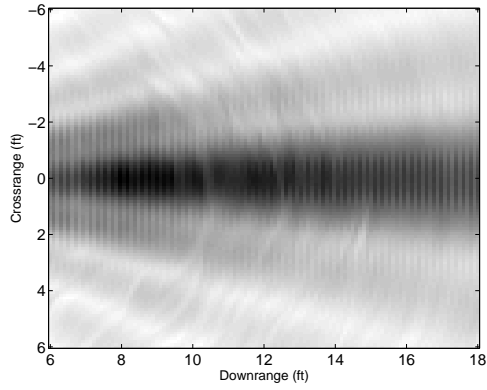
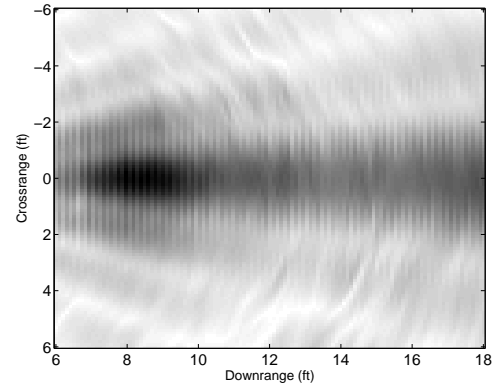
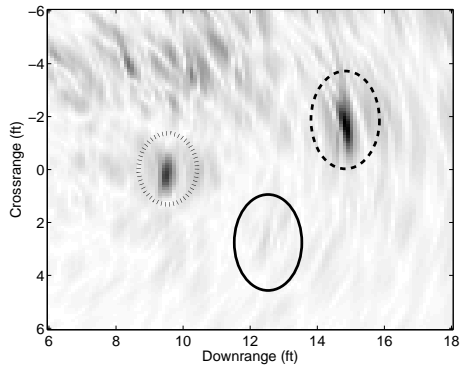
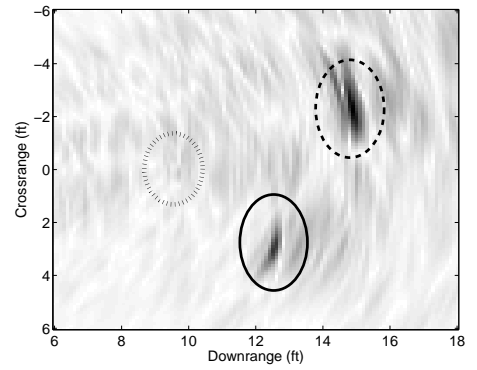
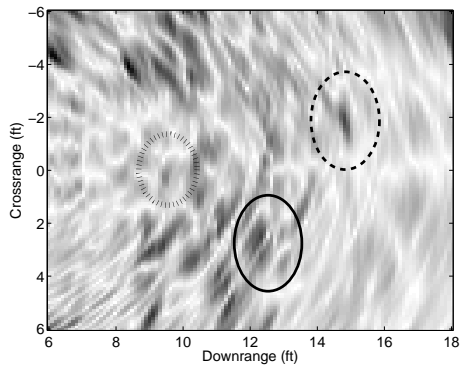
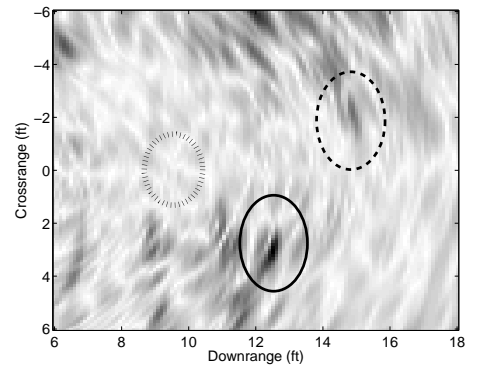
(a) B-Scan at height $-5in$, Raw data(b) B-Scan at height $+25in$, Raw data(c) B-Scan at height $-5in$, Background-subtraction(d) B-Scan at height $+25in$, Background-subtraction(e) B-Scan at height $-5in$, Wall removal(f) B-Scan at height $+25in$, Wall removal

Fig. 10. B-Scans obtained from wideband delay and sum beamforming

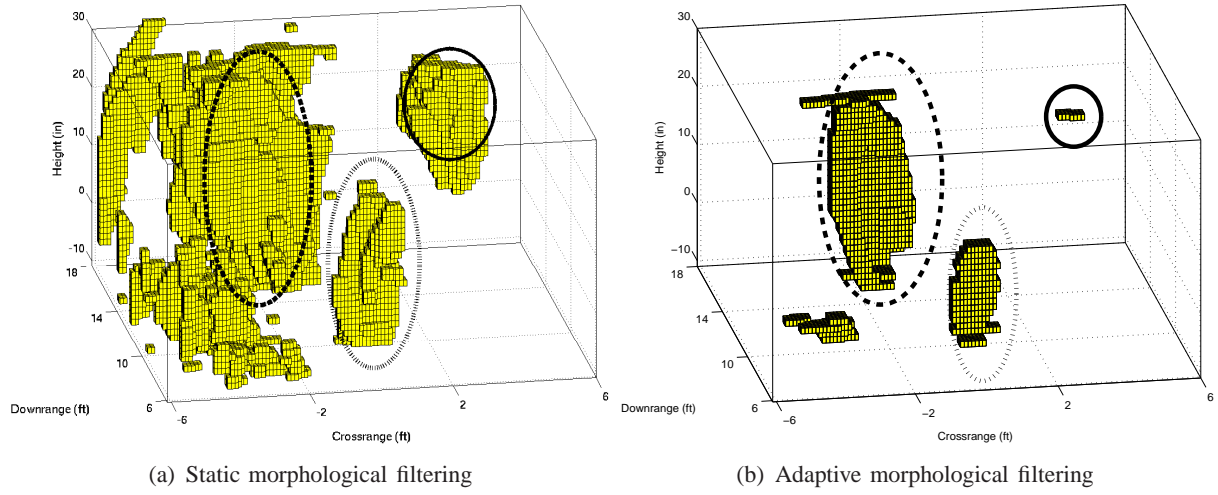


Fig. 11. 3D detection results using the iterative detector and background subtraction

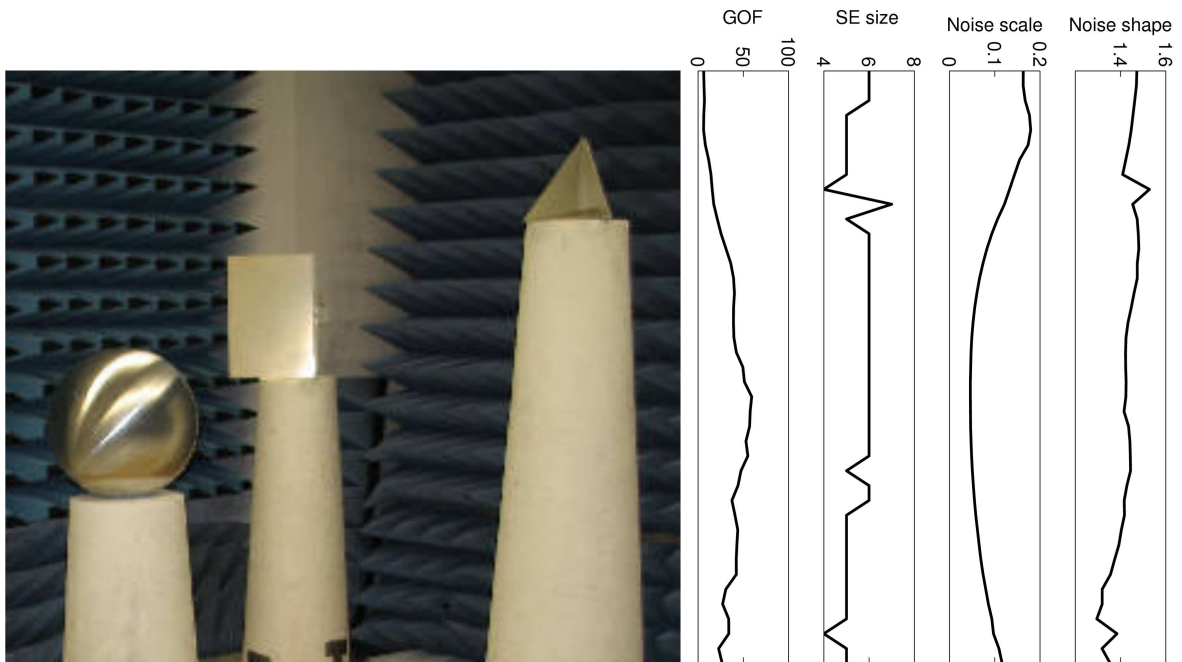


Fig. 12. Image statistics changing with height

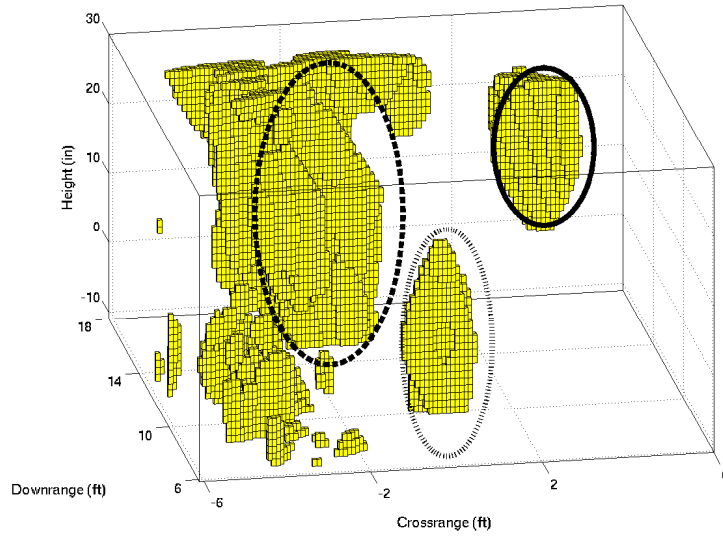


Fig. 13. 3D detection result, OSCFAR using background-subtraction

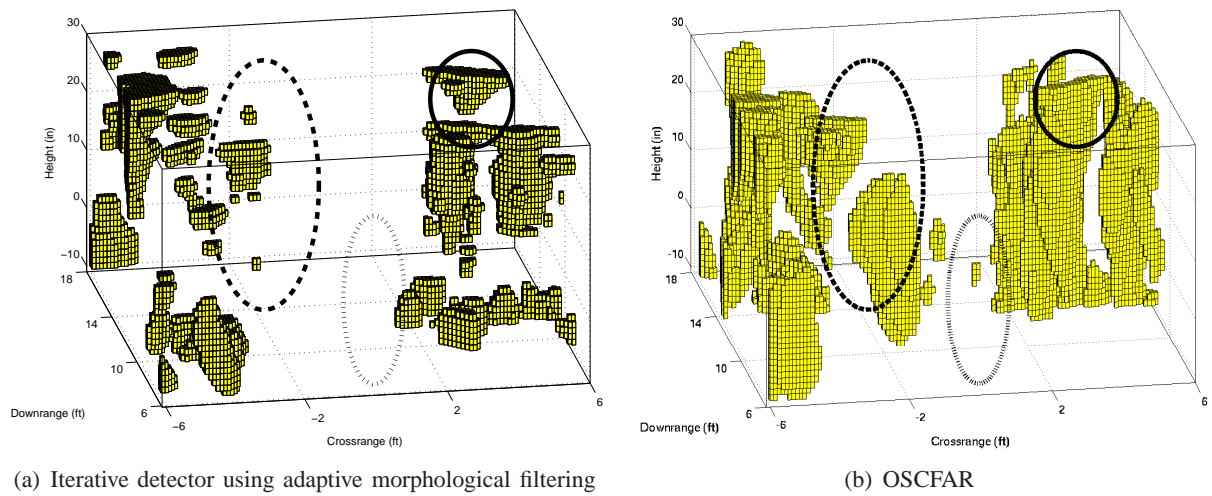


Fig. 14. 3D detection results using wall removal